Taylor-Couette-Poiseuille flow and heat transfer in an annular channel with a slotted rotor

Nicolas Lancial, Federico Torriano, François Beaubert, Souad Harmand, Gilles Rolland

Taylor-Couette-Poiseuille flow and heat transfer in an annular channel with a slotted rotor

Nicolas Lancial [a, *], Federico Torriano [b], François Beaubert [c], Souad Harmand [c], Gilles Rolland [a]

[a] EDF R&D, France
[b] Institut de Recherche d'Hydro-Québec, Varennes, Canada
[c] Université de Valenciennes, CNRS-LAMIH, Valenciennes, France

* Corresponding author.
E-mail address: nicolas.lancial@edf.fr (N. Lancial).

A B S T R A C T

This paper investigates a Taylor-Couette-Poiseuille flow in an annular channel of a slotted rotating inner cylinder, corresponding to a salient pole hydrogenerator. The purpose of this study is to improve the understanding of flow and thermal phenomena in electrical machines using a simplified scale model. The validation of the numerical model for a specific configuration is first shown by comparing the results with the experimental data. A parametric study is also performed to investigate all main flow regimes and to derive correlations in terms of the Nusselt number distribution on the rotor pole face and sides. The results show that the Nusselt number is proportional to the tangential Reynolds number to the power 1/7 in the pole and inductive faces trailing side. This relationship is similar to the one encountered in classical Taylor-Couette-Poiseuille flows between two concentric and smooth cylinders.

KEYWORDS
Hydrogenerator
Rotating machines
CFD
CHT
Heat transfer coefficient

1. Introduction

Salient pole synchronous machines convert the mechanical energy of water turbines into electrical energy. Although their efficiencies are greater than 95%, part of the mechanical energy available is lost in the form of heat. This heat must be efficiently evacuated to avoid overheating of the electrical components of the generator which can induce a rapid deterioration of the insulation material and, in some cases, lead to machine failure.

The cooling of a hydrogenerator is ensured by circulating a fluid (generally air) through the various generator components before it is directed toward a cooler where the heat is extracted. Understanding the flow dynamics and heat transfer mechanisms in the generator components (i.e., end-winding, pole face, etc.) is critical to ensure their efficient operation. To this end, experimental measurements on hydrogenerators can be performed. However, such measurements are costly, time-consuming and access to real machines is often limited.

Numerical tools such as Computational Fluid Dynamics (CFD) are increasingly used to characterize the thermofluid behaviour of large electrical machines. However, the geometric and flow complexity require the validation of simulation results from such numerical models which have not yet achieved a sufficient degree of maturity to be used alone.

The use of a laboratory scale model thus seems the best solution to acquire data for the validation of numerical models without the limitations associated with in situ measurements. This approach has been chosen by EDF (Électricité de France), LAMIH-CNRS (Université Lille Nord-de-France) and IREQ (Institut de Recherche d'Hydro-Québec), for whom a common strategy was established to share knowledge in the field of hydrogenerator thermofluid analysis.

Some experimental work has been undertaken in the past, but the majority of such studies have focused on only one particular component of the hydrogenerator. For example [9], developed an integral method to calculate the air flow rate across the coolers by scanning the flow with an anemometer. Furthermore [6], proposed an indirect method to measure the air flow across the coolers by applying the principle of conservation of energy in conjunction with measurements of the mass flow rate of the water, and the inlet and outlet temperatures of both fluids. More recently [10], performed measurements on a simplified model of a hydrogenerator

DOI : 10.1016/j.ijthermalsci.2016.09.022

Nomenclature

Latin symbols

$D_h = 2\frac{\pi(R_2^2-R_1^2)-nlp}{\pi(R_2+R_1)+np}$ Hydraulic diameter (m)
$e = R_2-R_1$ Air gap (m)
$Gr_{Dh} = g\beta\Delta T D_h^3/\nu^2$ Grashof number
h Heat transfer coefficient (W/m^2 K)
H Rotor height (m)
l Pole width (m)
n Number of poles
$Nu = hD_h/\lambda$ Nusselt number
p Pole depth (m)
R_1 Rotor radius (m)
R_2 Stator inner radius (m)
$Re_a = V_z D_h/\nu$ Axial Reynolds number
$Re_t = \omega R_1 D_h/\nu$ Tangential Reynolds number
$Ri_{Dh} = Gr_{Dh}/Re_{Dh}^2$ Richardson number
T Temperature (°C)
$Ta = \omega^2 R_1 \left(\frac{D_h}{2}\right)^3/\nu^2$ Taylor number
V_z Axial velocity (m/s)

Greek symbols

β Coefficient of thermal expansion (K^{-1})
θ Angle (°)
ν Kinematic viscosity (m^2/s)
ω Rotational speed (rad/s)
$\Gamma = H/D_h$ Elongation of the airgap (m)

to determine air flow rates across the stator and enclosure.

An experimental campaign was also carried out by Ref. [2] wherein the flow in static (cooler exit, pit opening, covers, and air gap) and rotating (interpole) components of a hydrogenerator scale model was characterized through particle image velocimetry (PIV) measurements. Some authors have performed experiments as well to determine heat transfer coefficients on active components of a generator. For example [5], obtained correlations between heat transfer coefficients on the leading and trailing faces of a salient pole and by comparing measured values with semi-empirical equations from earlier studies and found acceptable agreement. Moreover [22], performed heat transfer measurements on a salient pole generator and developed empirical correlations for the heat transfer coefficient on the pole sides and pole face. The authors found that, on the pole sides, heat transfer depends on the ratio of axial to tangential velocity (swirl parameter), whereas on the pole face it is mainly affected by the tangential velocity.

In a similar study by Ref. [19], temperature measurements on a four-pole synchronous generator were performed and equations for the heat transfer coefficient on the pole surface were derived. The local heat transfer coefficient was found to vary significantly across the pole surface and to be strongly related to the rotational speed. In another study by Ref. [8] aiming to measure the heat transfer correlations on the surface of a four-slots rotating cylinder placed in an annular channel, an axial speed and radial speed dependency was found, as well as a higher heat transfer on the leading edge than on the trailing edge of the rotor pole. More recently [12], demonstrated the validity of using an inverse algorithm to compute the time dependent heat flux on the rotor and stator surfaces of a high speed electric motor. Lastly [25], performed a hybrid numerical/experimental study to investigate (from temperature measurements) the heat transfer coefficient distribution on the pole face of a hydrogenerator scale model's rotor.

Recently, CFD has been used to tackle the problem of generator cooling and, although more computationally expensive than Lumped-Parameter Thermal Network (LPTN), it allows a more detailed and accurate analysis of the flow. For this reason, CFD is increasingly being used to improve the cooling efficiency of generators ([11]). Indeed [17,26], used it to simulate the cooling airflow and to determine convective heat transfer in different components. Furthermore [21], conducted a validation study by comparing measured and predicted local heat transfer coefficients. While the numerical model well predicted the overall trend of the heat transfer coefficient on the pole surface, the computed values were up to 30% lower than the measured ones. According to [23], more accurate results can be obtained using a Conjugate Heat Transfer (CHT) computation involving the coupling of flow and thermal simulations. Ref. [27] undertook such a study with a complete CHT analysis of a hydrogenerator and partially validated their results with experimental data.

This paper pursues the investigation of thermofluid phenomena in hydrogenerators that was undertaken by Ref. [16], namely the effect of a Taylor-Couette-Poiseuille flow on the heat transfer at the surface of a slotted rotating inner cylinder. The objective is to use CHT simulations to enrich the knowledge on flow and thermal transfer phenomena within electrical machines.

The present paper is subdivided into four sections. The scale model design is first presented. Then, the numerical models are detailed and validated for a specific configuration by comparing the results with the experimental data obtained from the scale model. Finally, a parametric study of flow regimes is performed and heat transfer correlations are extracted.

2. Scale model design

Understanding complex phenomena such as heat transfer in rotating parts of the machine is quite challenging, especially considering the limited experimental data due to restricted access and difficulties of performing measurements on actual generators.

Such data can serve to validate numerical models that allow a better comprehension of thermal and flow dynamics in generators. For this reason, a hydrogenerator scale model was designed and built at EDF/LAMIH-CNRS. This model is a simplified version of generators prototypes in EDF production plants, since it lacks active electromagnetic elements. Thus, the thermal analogy compared to a real configuration is not fully respected (especially in the notch region). Using the EDF/LAMIH-CNRS scale model of a hydrogenerator, temperatures on the rotor pole face can be measured and then compared with the numerical values obtained from Ansys-CFX, and *Code_Saturne 3.0* coupled with SYRTHES 4.0. After validating the numerical models, a parametric study is performed to investigate all main flow regimes and to derive correlations for the Nusselt number distribution on the rotor pole face and sides.

As illustrated in Fig. 1, the scale model is in an open loop ventilation circuit. The air is driven by a fan and is directed by two static air guides located upstream and downstream of the rotor/stator system. The main simplifications in the scale model include the omission of the coils and the ducts in the stator. It can be noted that the geometry has a periodicity of 1/10.

The stator is a transparent cylindrical plate comprising a flat

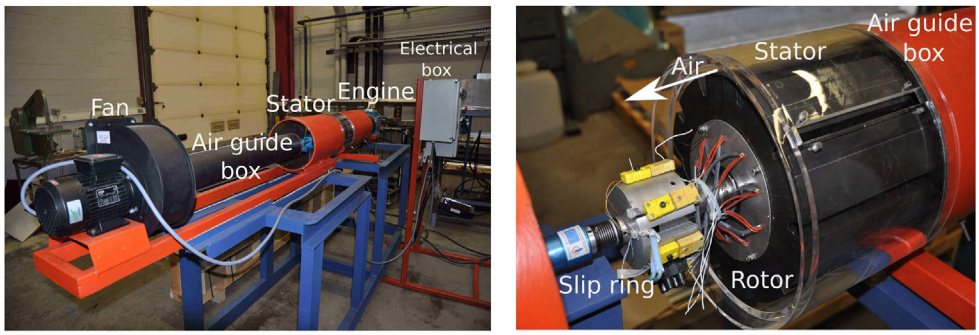

(a) Full view of the scale model.

(b) View of the rotor and stator, the latter is removable and made of Lexan.

Fig. 1. Generator scale model.

section (made of fluorine, 0.186 m × 0.016 m, τ=0.88) that allows optical access to the rotor components and avoids optical aberration for the IR FLIR SC7200-MB thermal imaging camera and for flow visualization with Particle Image Velocimetry (PIV).

The acquisition frequency of the IR camera is 500 Hz, allowing sufficient time resolution. A uni-directional hot wire probe is used to measure axial velocity at $6D_h$ upstream of the rotor/stator system and to obtain inlet boundary conditions for the numerical simulations. Its sampling frequency is 1 kHz.

The rotor tip is driven by an ABB 1.1 kW engine. Table 1 and Fig. 2 show the main scale model characteristics.

The rotor is made of steel and turns clockwise up to a maximum speed of 1500 rpm (± 1 rpm) and the maximum tangential velocity at the rotor blade is 18.7 m/s. The fan can generate an axial air velocity up to 10 m/s, giving a range of flow regimes of $0 \leq Re_a \leq 14250$ and $0 \leq Ta \leq 1.7 \times 10^7$. The objective was to maintain prototype-model similitude with regard to the Reynolds number in the hydrogenerator air gap. The Mach number is below 0.3, meaning that the flow can be considered incompressible.

The overall dimension has been scaled down (1:6 in the radial direction and 1:12 in the axial direction) and the main components have been dimensioned to maintain similarity with the prototype for the following parameters: $\frac{p}{l}$, $\frac{R_1}{p}$ and $\frac{H}{R_1}$. The hydraulic diameter is calculated using the following equation, $D_h = 2\frac{\pi(R_2^2-R_1^2)-nlp}{\pi(R_2+R_1)+np} = 0.02289$ m.

The scale model can be used to analyse heat transfer phenomena occurring on the surface of a rotor pole. In order to perform surface temperature measurements with the IR camera, the rotor is painted in black and has an emissivity ε=0.9. A slip ring on the rotor shaft connects 10 cartridge heaters to a power source. Each heater has a maximum output of 300 W and is equipped with a J-type thermocouple. A transformer is used to regulate the injected power and to obtain a steady temperature.

Temperatures inside the scale model are measured with K-type thermocouples (±1.5 °C) and are acquired by a two-channel slip ring connected to a data logger system.

The operating air temperature in the enclosure can exceed 30 °C due to heat generated by windage losses and the cartridge heaters. Sufficient cooling is provided to maintain temperatures around 70 °C in the rotor pole.

Table 1
Scale model characteristics.

Characteristics	Dimensions
Rotor radius, R_1	119 mm
Rotor height, H	186 mm
Pole width, l	55 mm
Pole depth, p	20 mm
Air gap, e	10 mm
Number of poles, n	10
Stator inner radius, R_2	129 mm

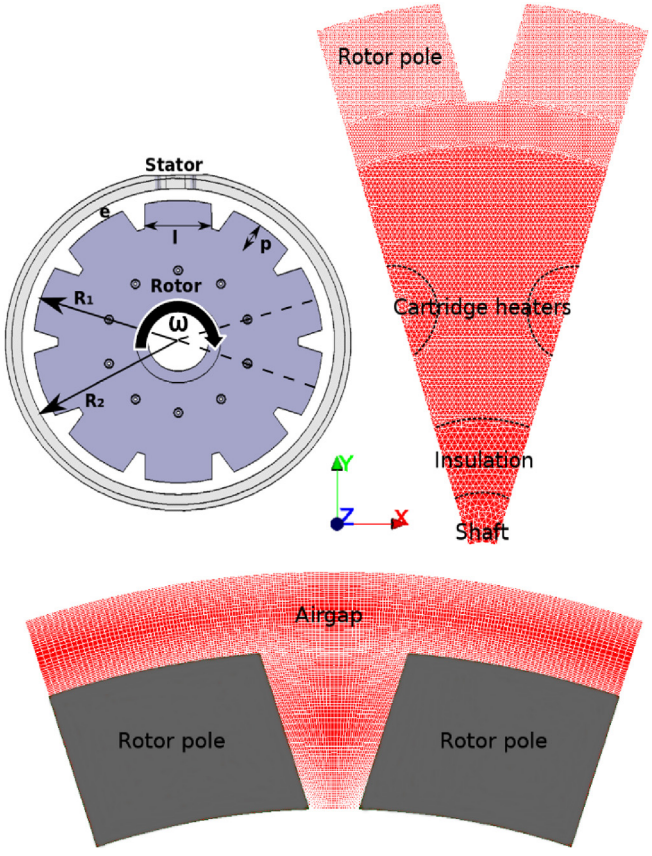

Fig. 2. CAD model and its mesh used in numerical calculations.

3. Numerical model

In this study, the temperature distribution is computed through CHT simulations by calculating heat transfer in the solid and fluid domains involving CFD and thermal computations, using open-source EDF softwares *Code_Saturne* and SYRTHES 4.0, respectively. The software Ansys-CFX was also used to benchmark numerical results. As presented in Fig. 2, the CAD model is based on an

industrial hydrogenerator and includes the rotor and the stator. The mesh is generated with the open-source EDF software platform SALOME 6.6. The hexahedral fluid mesh and the tetrahedral solid mesh have 4,431,900 cells and 5,400,000 cells respectively. A mesh independence study was performed for both domains to ensure appropriate grid resolution.

Considering the use in this study of the k-ω Shear Stress Transport (SST) model, the mesh refinement near the no-slip walls was set to obtain a y^+ value close to 1. A SIMPLEC algorithm is used for the pressure-velocity coupling. A rotating motion is applied to the full domain so that additional rotational effects (Coriolis and centrifugal terms) are included.

For the two air guide boxes, which are stationary, a counter-rotating velocity was set to ensure a static wall in the absolute reference frame. Compared to the experimental scale model, the downstream air guide box was artificially extended in order to limit the effect of the pressure outlet boundary condition. The solid domain includes the rotor, the cartridge heaters, the insulation and the shaft. A volumetric heat source is applied inside the cartridge heaters. A similar mesh size was specified at the fluid/solid interface.

For unsteady calculations, a second order Crank-Nicholson scheme with a time step of 5×10^{-5} s (CFL $\simeq$ 2) was set. For both steady and unsteady calculations, a second-order discretization scheme in space was used. Convergence was reached when all RMS residuals were below 10^{-5}.

As the thermal time scale is much higher than the fluid time scale, the solid and fluid problems can be resolved independently according to Ref. [7]; therefore, weak coupling can be used. Indeed, the flow is not much affected by the thermal conditions (i.e., temperature is a passive scalar) since the Richardson number Ri_{Dh} for the validation case is close to 0.035 and consequently forced convection is predominant. The CHT calculation can thus be performed using the following procedure: a time-averaging of the global fluid variables is first performed and then the average flow field obtained from the CFD calculation is used to compute the temperature distribution in the solid and fluid domains simultaneously by solely solving the energy equation. The coupling at the interface between the two domains is achieved through fitting boundary conditions. Convergence in SYRTHES and Ansys-CFX was reached when the RMS energy residual was below 10^{-6} and when all monitor points values were stable. The unsteady calculations based on the coupling between *Code_Saturne* and SYRTHES took, on average, 8 days using 180 cores of the EDF Ivanoe cluster.

4. Results and analysis

4.1. Preliminary numerical tests

The influence of numerical parameters is studied in this section. The objective is to select the most suitable numerical method allowing an optimal balance between the computational cost and the accuracy of the results.

Some preliminary numerical tests have been performed to investigate the possibility of using a steady state analysis, the influence of the computational domain with or without periodic conditions, the influence of rotor/stator interfaces and of the turbulence models ([16]). For these sensitivity studies, no axial velocity was applied and the rotational speed was set to $\omega = 500$ rpm, unless otherwise specified. It should be noted that a steady state solution can be obtained only for $\omega \leq 2.09$ rad/s, when no axial velocity is applied.

However, as the majority of the numerical computations performed in this study are at higher rotational speeds, an unsteady solver had to be used and the influence of the integration period on the mean flow values had to be investigated. To do so, once the fully periodic regime was reached, the mean quantities were averaged over different periods of time. The results show a difference of 2% between the values averaged over a time period of 6 s and 13 s. The characteristic time was $T_\omega = \frac{D_h}{\omega R_1} = 0.0037$ s and thus an integration time of 6 s corresponded to 1622 T_ω.

Regarding the influence of periodic boundary conditions, a comparison between the periodic and full domains indicated a good similarity between the results. Indeed, a maximum error of 5% is observed between the two cases for the axial velocity distribution along the axial and radial directions at the middle of the rotor. Thus, all subsequent simulations can be run with a periodic domain.

Several turbulence models have also been tested: low-Reynolds (k-ω SST, v2f-BL-v2/k and Rij-EBRSM) and high-Reynolds models (k-ε and Rij-SSG). The overall mesh size used is 4,431,900 elements for low-Reynolds models. A separate mesh (124,350 elements) was used for high-Reynolds models ($y^+ \simeq 30$). Differences can be observed between the low and the high-Reynolds models for all flow variables. However, no obvious differences were observed between the first order (k-ω SST, v2f-BL-v2/k) and second order (Rij-EBRSM) low-Reynolds models. Similar conclusions were drawn for the high-Reynolds models (k-ε, Rij-SSG).

Considering the importance of the flow behaviour in the near-wall region as it dictates the heat transfer mechanism at the rotor surface, a low-Reynolds k-ω SST model was preferred.

4.2. Comparison between experimental and numerical results

The CHT simulations are performed with two CFD software codes: *Code_Saturne 3.0* coupled with the thermal software SYRTHES 4.0 and Ansys-CFX. Table 2 shows the main numerical computation characteristics and Table 3 presents the boundary conditions used for this validation case.

The domain inlet is placed at $6D_h$ upstream of the rotor/stator system and the velocity profile obtained from hot wire measurements was specified here as boundary condition. At the demain outlet, a constant pressure condition (relative pression of 0 Pa) is specified. The operating air temperature was approximately 21 °C.

Fig. 3 shows the different studied areas of the rotor: the leading edge on the rotor left side and the trailing edge on the right side. The pole faces are located at the highest radius of the rotor whereas the notch is found at the lowest radius.

The comparison of the normalized temperature contours is presented in Fig. 4. Some experimental approximations are unavoidable due to the use of the IR camera from the stator window, especially close to the rotor ends and between each window measurement. To account for this, grey bands are placed in the regions where an interpolation was performed.

Table 2
Main numerical parameters.

	Fluid domain	Solid domain
Discretization method	Finite volume	Finite element
Mesh type	Hexahedral	Tetrahedral
Mesh conception	Structured block ($y^+ \simeq 1$)	Structured block
Total elements	4,431,900	5,400,000

Table 3
Main boundary conditions of the validation case.

Power (W)	V_z (m/s)	Re_a	ω (rad/s)	Re_t	Ta
507.6	2	3115	52.36	9710	2,332,610

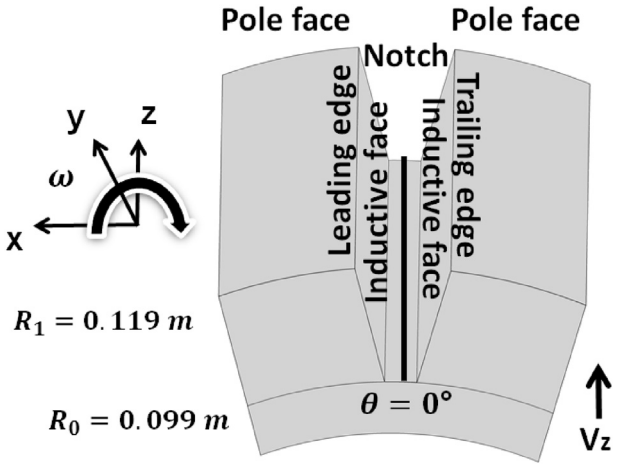

Fig. 3. Different studied areas of the rotor.

The two codes accurately predict the rotor temperature distribution since the hot spot temperature is about 0.9 °C higher for Ansys-CFX and 1.2 °C lower for SYRTHES compared to experimental data, as shown in Table 4. Moreover, as illustrated in Fig. 5, the experimental temperature profiles along $z/H = 0.5$ and $\theta = 0°$ lay between SYRTHES and Ansys-CFX results.

It is interesting to mention that typically hydrogenerators can withstand a maximum operating temperature of 130 °C, due to the type of insulation materials (class B) used inside these machines.

The temperature contours of Fig. 4 show that the pole leading side is better cooled than the trailing side due to a greater impingement of the flow on the former surface, in contrast to a large recirculation region present near the trailing side wall, as it can be seen in Fig. 6.

Moreover, an axial temperature gradient is present along the pole surface and the minimum pole surface temperature is found

Table 4
Comparison between experimental and numerical hot spot temperature and position values along $\theta = 0°$.

Hot spot	T (°C)	Position (z/H)
Experimental	71.1	0.82
SYRTHES	69.8	0.79
Ansys-CFX	71.9	0.83

on the bottom corner of the leading edge. The flow generated by the axial fan in the positive z-direction caused this distribution to occur with the presence of cooler air at the entrance of the notch region. Inversely, the hot spot is located at the downstream end of the rotor notch due to the presence of low flow velocities in this region (see Fig. 6) and to the fact that the cooling fluid has been warmed by its passage along the heated pole surfaces.

The isosurface of azimuthal vorticity in Fig. 6 illustrate the presence of a strong vortex in the notch region, generated at the upstream end of the pole trailing edge and extending up to 3/4 of the pole length. A secondary vortex starts at the upstream end of the pole leading corner and is diagonally convected along the pole, due to the presence of an axial velocity component.

The presence of the latter vortex causes a decrease in the heat transfer coefficient, as shown in Fig. 7 by the indent near $\theta = 5°$ and $\theta = -12°$ on the lines located at $z/H = 0.027$ and $z/H = 0.25$, respectively. The presence of these vortices is predicted by both numerical codes, although they seem to dissipate slightly faster with Ansys-CFX. The decrease in the Nusselt number profiles from the leading edge to the trailing edge of the pole face shown in Fig. 7 has previously been observed by Refs. [8,25].

In the notch region, the Nusselt number profiles are quite uniform in the circumferential direction θ with values similar to those observed near the trailing edge of the pole, except for the profiles located at $z/H = 0.027$ and $z/H = 0.25$. Indeed, near the notch entrance region, a large recirculation zone adjacent to the pole trailing edge is observed (as presented in Fig. 6). Finally, the Nusselt

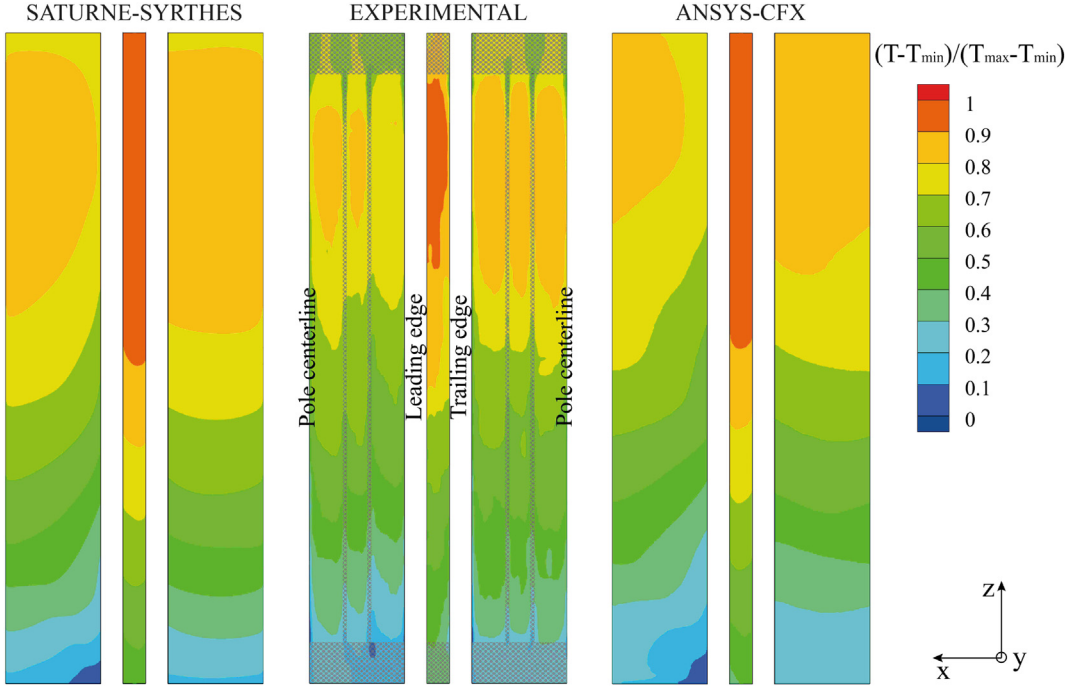

Fig. 4. Normalized temperature contours on the pole face, obtained from experimental and from numerical data.

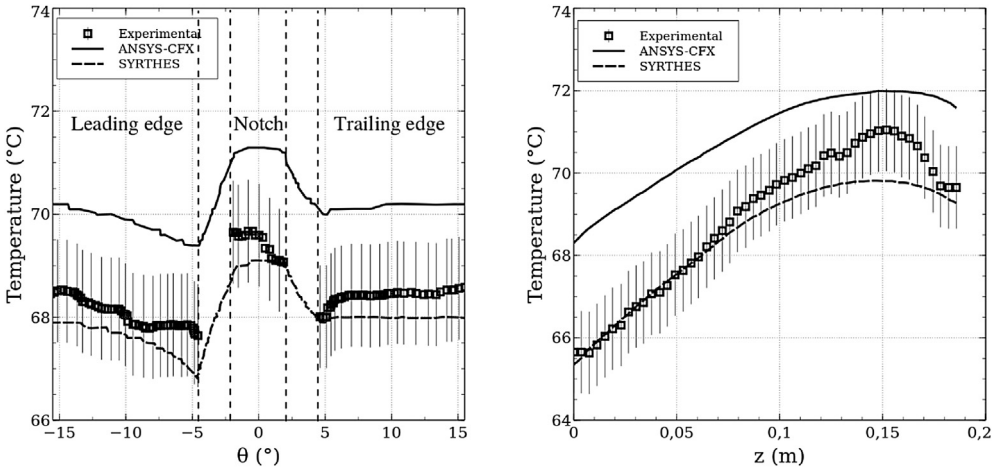

(a) $z/H = 0.5$. (b) $\theta = 0°$.

Fig. 5. Experimental and numerical temperature profiles at $z/H = 0.5$ and $\theta = 0°$.

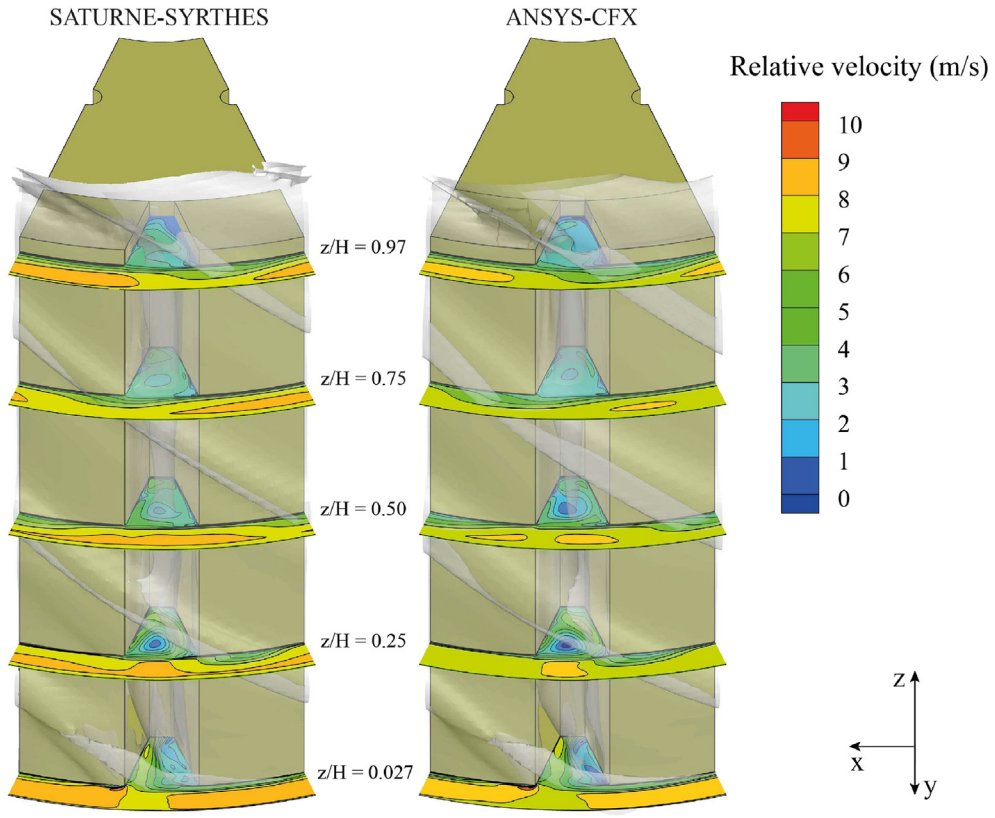

Fig. 6. Relative velocity contours and isosurface of azimuthal vorticity along the air gap and notch regions.

number on the pole face and in the notch region decreases with increasing z due to the growth of thermal boundary layers.

In summary, the CHT simulations performed with Saturne-Syrthes and Ansys-CFX have predicted a temperature distribution quite close to the measured one, allowing extrapolation of the Nusselt number profiles on the pole face. Overall, the values given by the two codes are in good agreement except at $z/H = 0.027$ where *Code_Saturne* predicts a significantly higher heat transfer coefficient. This is not so surprising since even a small change in the dynamics of the pole leading edge tip vortex (see Fig. 6) can greatly affect the local heat transfer. This comparison has validated both numerical codes, and a parametric study of the flow regimes can now be performed.

4.3. Effect of flow regimes on hot spot

In this section, the effects of flow regime on hot spot value and location are studied. Note that here the losses are not representative of those found in real electrical machines, where they are mainly present in the inductive face. Table 5 presents the

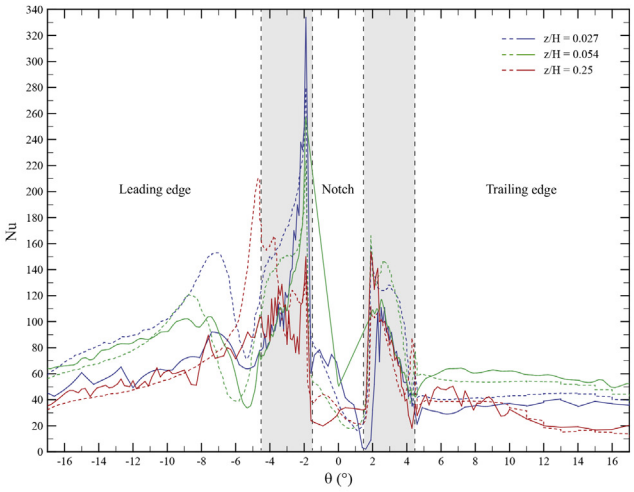

(a) Nusselt number profiles at the upstream end of the pole face.

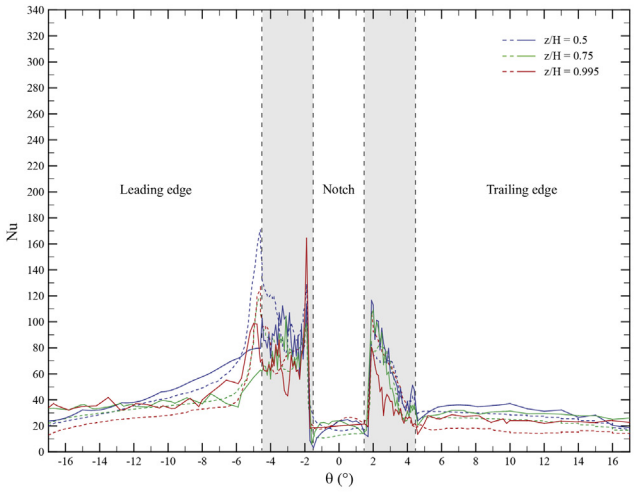

(b) Nusselt number profiles at the downstream end of the pole face.

Fig. 7. Nusselt number profiles on the pole face (Ansys-CFX: solid lines; SYRTHES 4.0: dashed lines).

Table 5
Parametric study.

Power (W)	Re_t	Ta	Re_a		
507.6	195	938	779	3115	6235
	972	23,360			
	1940	93,270			
	9710	2,332,610			
	29,130	20,993,510			

parameters of the different flow regimes that have been investigated.

4.3.1. Predominance of axial velocity on rotational velocity

Fig. 8 presents laminar and turbulent flow regimes where the axial velocity predominates over rotational velocity. The flow is not perturbed within the notch region. Consequently, the temperature and Nusselt number distributions are symmetric with respect to $\theta = 0°$. As expected, near the notch entrance region, a better cooling can be observed. The axial Nusselt number distribution is more uniform for the laminar regime.

4.3.2. Predominance of rotational velocity on axial velocity

Fig. 9 presents respectively laminar and turbulent regimes with vortices where the rotational velocity predominates over the axial velocity. In this case, the flow is highly perturbated in the notch region where a strong vortex is observed. Consequently, the temperature and the Nusselt number distributions become asymmetric with respect to $\theta = 0°$.

The axial velocity stabilizes the flow and delays or prevents the creation of vortices in the notch region. In contrast, the rotational speed promotes the formation of vortices in the notch region (as shown in Fig. 9), that cause a cooling imbalance between the leading and trailing sides of the pole. This phenomenon was also observed by Ref. [4] and by Ref. [8].

4.4. Hot spot position and temperature for all studied cases

Fig. 10 shows the evolution of the hot spot temperature (a) and its position P_{Tmax} along z/H (b) as a function of Re_a and Re_t. Some remarks can be made:

- The maximum temperature decreases with increasing Re_a and Re_t,
- if the axial Reynolds number Re_a is predominant, the hot spot temperature tends to be independent of rotational velocity. Moreover, for a weak tangential velocity ($Re_t = 195$), the axial velocity has a large impact on the rotor cooling,
- if the rotational Reynolds number Re_t is predominant, a strong reduction of hot spot temperature with increasing rotational velocity is observed, especially for weak axial velocities ($Re_a = 779$). An increase of the rotational velocity tends to shift the hot spot toward the downstream end of the rotor, as illustrated in Fig. 10b.

4.5. Nusselt number variation

The different flow regimes studied in the current confined rotating cavity are summarized in Fig. 11 and four different regions can be noted:

- Regime I: Laminar ($0 \le Re_a \le 779$, $0 \le Re_t < 972$),
- Regime II: Laminar with vortices ($0 \le Re_a \le 779$, $972 \le Re_t$),
- Regime III: Turbulent ($3115 \le Re_a \le 6235$, $0 \le Re_t \le 1940$); ($6235 \le Re_a$, $0 \le Re_t \le 9710$),
- Regime IV: Turbulent with vortices ($3115 \le Re_a \le 6235$, $1940 \le Re_t$); ($6235 \le Re_a$, $9710 \le Re_t$).

A blank region is present in the graph as no numerical case has been treated close to $Re_a = 2000$. However, in an industrial context $Re_t \simeq 750\,000$ and $Re_a \simeq 30\,000$ and it can be assumed that a turbulent flow with vortices would be present. Before looking in more detail at the influence of the axial or tangential Reynolds number, some comparisons can be made with the literature to determine whether the variation in the global Nusselt number in the different areas of the rotor is similar to the one found in previous studies.

The comparisons are given in Fig. 12 for $\overline{Nu_{rotor}}$, which is the average Nusselt number computed on the whole rotor surface.

Several authors have been chosen to compare data based on the same range of axial and tangential Reynolds numbers, namely the data given by Refs. [24,14] (with smooth rotor and stator) [4], (with slotted stator and smooth rotor) and [8] (with slotted rotor and

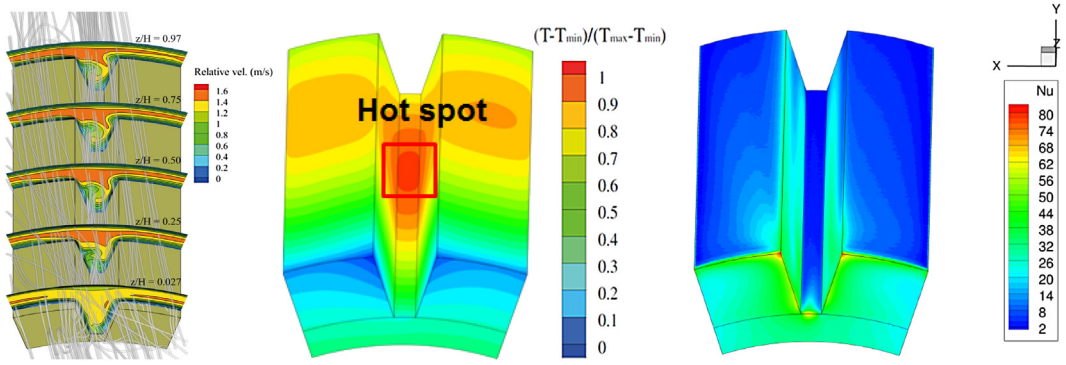

(a) Laminar ($Re_a = 779$, $Re_t = 195$).

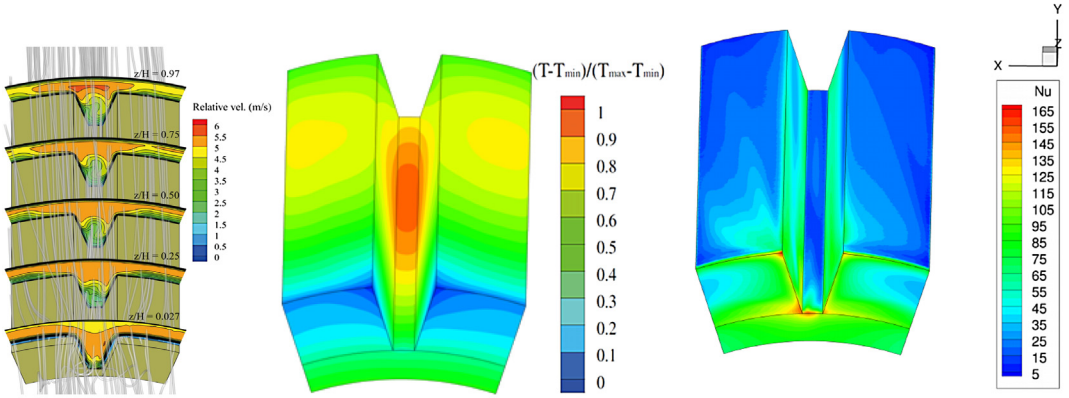

(b) Turbulent ($Re_a = 3115$, $Re_t = 195$).

Fig. 8. Predominance of axial velocity on rotational velocity.

smooth stator).

While this comparison reveals some differences, the values from all studies show the same order of magnitude. In the present case, the value of $\overline{Nu_{rotor}}$ is higher than in the previous studies with a slotted rotor. This difference can be explained by the fact that the fully developed regime is not reached in the current case and thus higher Nusselt number values are observed.

Moreover, the studied geometries are quite different, especially with the respect to the ratio $\Gamma = H/D_h$. In fact, the value of Γ is 7.9 in the present study whereas it is close to 14 in Ref. [14], where a lower Nusselt number is observed. The same observation can be made in comparison to [8], where once again a higher ratio $\Gamma = 31.6$ leads to a lower Nusselt number.

One particular case can be noted, especially for $Re_a = 6235$ where the Nusselt number is not affected by the rotational velocity up to $Re_t \simeq 1940$. This phenomenon was also observed by Ref. [8] and it implies that the critical Taylor number, Ta_c, has not been reached yet. The value of Ta_c is related to the formation of vortices in the rotor notch, which can be observed through CFD simulations. Overall, the local Nusselt number rises with increasing axial and tangential Reynolds numbers. Table 6 shows the average Nusselt numbers on different rotor components. The cases without rotational velocity ($Re_a = 3115$, $Re_t = 0$) and without axial velocity ($Re_a = 0$, $Re_t = 9710$) are also presented.

From this data, some remarks can be made:

- If Re_a is fixed, the Nusselt number quickly rises with higher rotational velocity (especially for $Re_t \geq 9710$),
- if Re_t is fixed, the Nusselt number increases almost linearly with increasing axial velocity,
- when $Re_t > 0$, the leading side of the rotor pole is for all cases better cooled than the trailing side and the inductive faces are better cooled than the pole faces,
- the Nusselt number seems to slowly increase with Re_a in the rotor notch, except for high rotational velocities where the Nusselt number increases rapidly.

The Nusselt number depends on Re_a and Re_t, but also on z/D_h since the fully developed regime is not reached in the current study. Some authors consider an effective Reynolds number as $Re_{eff} = (Re_a^2 + \alpha \times Re_t^2)^{1/2}$, with a constant α to combine the two effects of an axial and tangential velocity.

In the present case, a global correlation for the Nusselt number is computed for all studied flow regimes, meaning that Re_a and Re_t have to be taken separately. This correlation can thus be approximated in terms of power law as:

$$Nu = A \times Re_a^n \times Re_t^m \times \left(\frac{z}{D_h}\right)^o \quad (1)$$

where n, m and o are constants and $\frac{z}{D_h}$ is the dimensionless rotor length.

4.5.1. Pole face leading and trailing sides

By using the least squares method, as proposed by Ref. [8], the following values are obtained: $A = 0.1$, $n = 0.51$, $m = 0.26$ and $o = -0.23$ for the pole face leading side and $A = 0.04$, $n = 0.66$, $m = 0.16$ and $o = -0.12$ for the pole face trailing side.

In the literature [20,4], have found a coefficient close to 0.8 using Re_{eff}, whereas Ref. [8] has found a value equal to 0.62. Regarding the

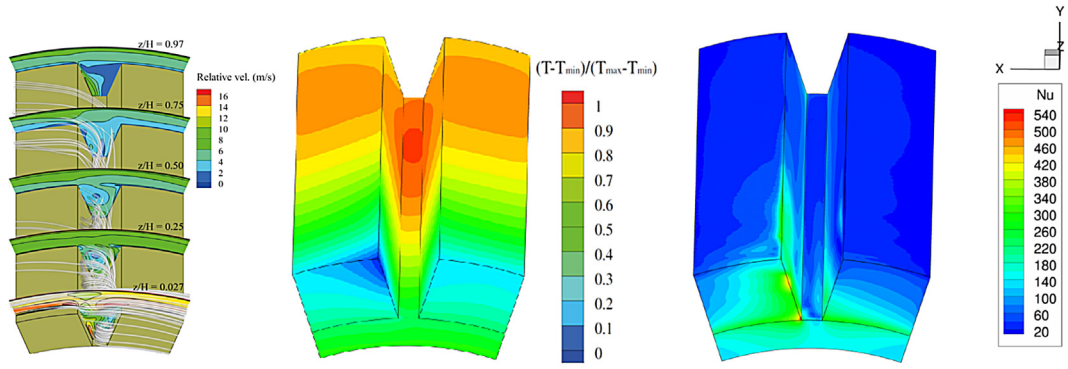

(a) Laminar with vortices ($Re_a = 779$, $Re_t = 29130$).

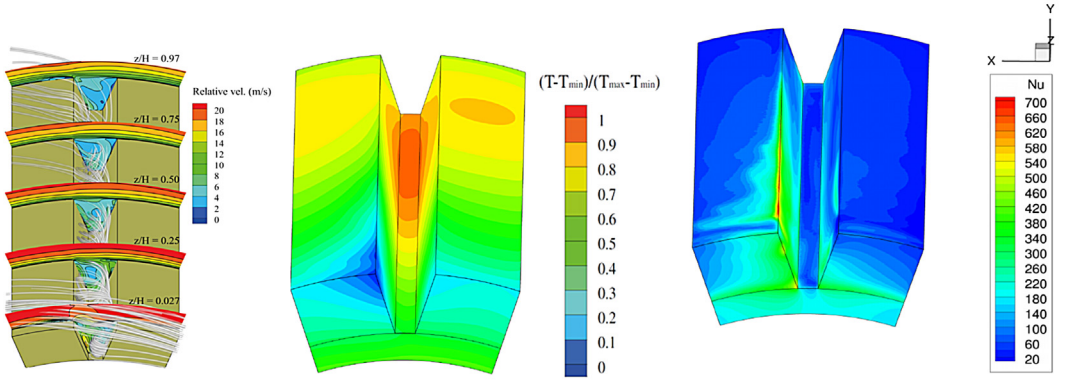

(b) Turbulent with vortices ($Re_a = 3115$, $Re_t = 29130$).

Fig. 9. Predominance of rotational velocity on axial velocity.

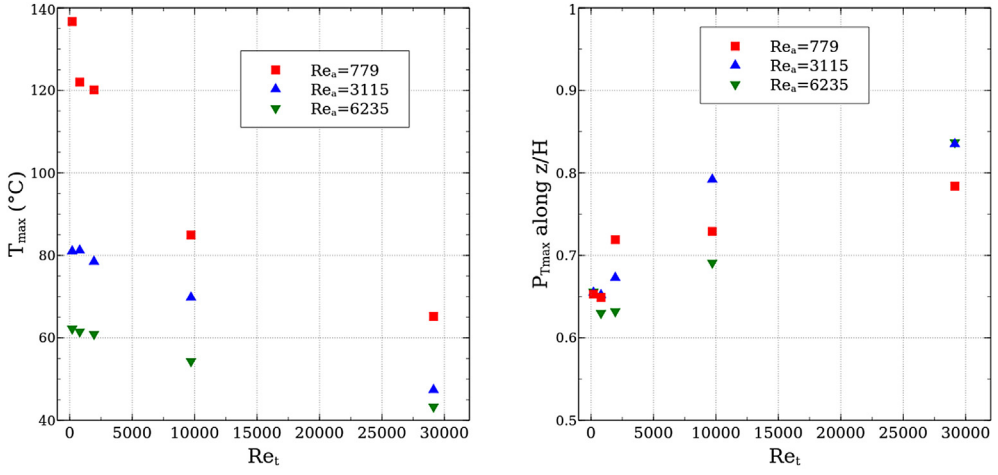

(a) Evolution of T.

(b) Evolution of $P_{T_{max}}$ along z/H.

Fig. 10. Evolution of the hot spot temperature and its position according to Re_a and Re_t.

value of o, it is also quite different from the values found in the literature ($o = -0.44$ for [8] and $o = -0.451$ for [18]).

The main differences compared to [8] are:

- In the present study, the Nusselt number is calculated on the leading and trailing sides separately, whereas in Ref. [8], it is calculated by taking into account both sides,
- the laminar regime is considered in the present study,
- the fully developed flow is not reached in this study.

Moreover, the Nusselt number, especially for the pole face trailing side, depends on Re_t to the power 0.16. Ref. [1] obtained from their experiment an exponent of 0.13, which is close to the 1/7 value predicted analytically from the turbulent boundary layer theory for concentric and smooth cylinders. The same authors also found a coefficient of 0.77 for the axial Reynolds number, which is close to the value found in the present study for the pole face trailing side (0.66).

Since in an actual hydrogenerator a fully developed flow is

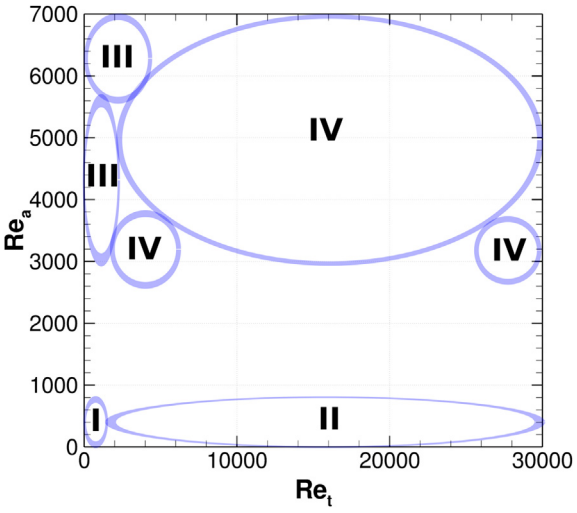

Fig. 11. Demarcation lines of the different flow regimes studied in the slotted confined rotating cavity.

generally not reached, the following global correlations can be used for $780 < Re_a < 6250$ and $200 < Re_t < 29100$ (i.e., $940 < Ta < 21{,}000{,}000$):

$$Nu_{pole_{lead}} = 0.1 \times Re_a^{0.51} \times Re_t^{0.26} \times \left(\frac{z}{D_h}\right)^{-0.23} \quad (2)$$

$$Nu_{pole_{trail}} = 0.04 \times Re_a^{0.66} \times Re_t^{0.16} \times \left(\frac{z}{D_h}\right)^{-0.12} \quad (3)$$

The average relative error is about 21.6% for the leading side and 31.5% for the trailing side by comparing each correlation with the values obtained from Table 6.

4.5.2. Inductive face leading and trailing sides

As it was observed for the pole face, the Nusselt number varies in terms of Re_a, Re_t and z/D_h. By applying the least squares method in the inductive face leading and trailing sides, new coefficient values can be obtained: $A = 0.35$, $n = 0.46$, $m = 0.26$ and $o = -0.2$ for the leading side and $A = 0.23$, $n = 0.57$, $m = 0.16$ and $o = -0.18$ for the trailing side. The coefficient associated to the Reynolds number is generally close to 0.8 in the literature, when considering Re_{eff} ([4,14,20]). According to Ref. [8], this coefficient value is equal to 0.77. Furthermore, the Nusselt number, especially for the inductive face trailing side, depends on Re_t to the power of 0.16, similar to the theoretical exponent of 1/7 for concentric and smooth cylinders, according to Ref. [1]. For the axial Reynolds number, the same authors found a correlation of 0.77, which is quite close to the value found in the present study for the inductive face trailing side (0.57).

From the current study, the global correlations for the Nusselt number for $780 < Re_a < 6250$ and $200 < Re_t < 29100$ (i.e., $940 < Ta < 21{,}000{,}000$) are:

$$Nu_{inductive_{lead}} = 0.35 \times Re_a^{0.46} \times Re_t^{0.26} \times \left(\frac{z}{D_h}\right)^{-0.2} \quad (4)$$

$$Nu_{inductive_{trail}} = 0.23 \times Re_a^{0.57} \times Re_t^{0.16} \times \left(\frac{z}{D_h}\right)^{-0.18} \quad (5)$$

The average relative error is about 21.2% for the leading side and 22.4% for the trailing side, when comparing with values of Table 6.

Other configurations can also be compared to our study, such as a rotating tube ([3]) or a rotating slotted cylinder ([8]), as illustrated in Fig. 13.

For low tangential Reynolds numbers ($Re_t < 9710$), the literature values are close to those found in the current study, especially for the trailing side. Indeed, a different behaviour can be observed between the two sides of the inductive face: the value of Nu increases with Re_t in the leading side whereas it decreases in the trailing side. For higher Re_t ($Re_t \geq 9710$), the Nusselt number rises with increasing Re_t whereas it tends to be constant according to [8]. The evolution of the Nusselt number in the present study is similar to that found in a rotating tube, especially for the trailing side of the inductive face.

4.5.3. Notch

Once again, the Nusselt number varies with Re_a, Re_t and z/D_h. By using the least squares method in the notch region, the following coefficient values can be obtained: $A = 0.02$, $n = 0.69$, $m = 0.27$ and $o = -0.35$. Regarding the value of o, it is close to the values found in the literature ($o = -0.44$), according to Refs. [8,18].

The global correlation for the Nusselt number for $780 < Re_a < 6250$ and $200 < Re_t < 29100$ (i.e., $940 < Ta < 21{,}000{,}000$) then becomes:

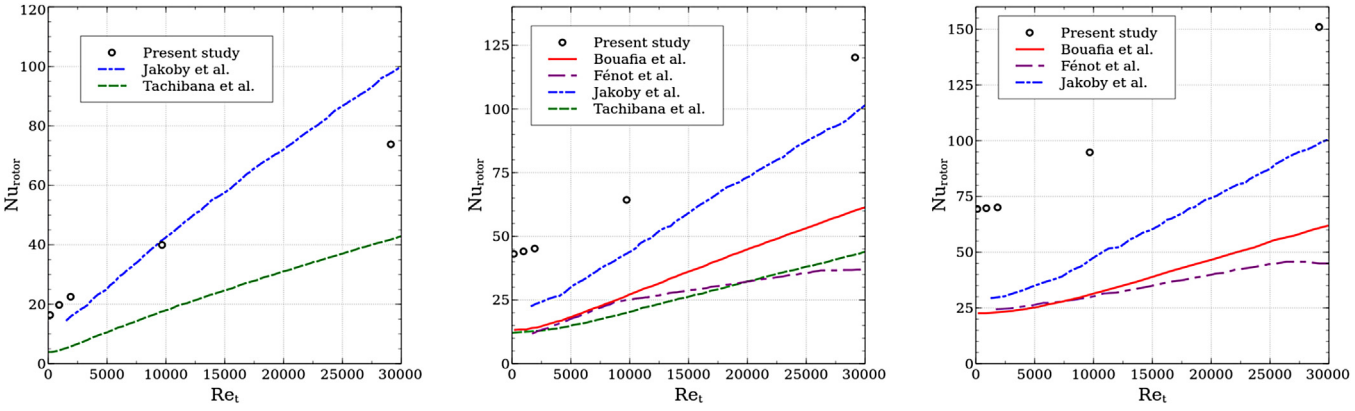

(a) Axial Reynolds number: $Re_a = 779$. (b) Axial Reynolds number : $Re_a = 3115$. (c) Axial Reynolds number : $Re_a = 6235$.

Fig. 12. Evolution of the average Nusselt number as a function of Re_t.

Table 6
Average Nusselt number obtained in the different parts of the rotor as a function of Re_a and Re_t.

Re_a	Re_t	$Nu_{pole_{lead}}$	$Nu_{ind_{lead}}$	Nu_{notch}	$Nu_{ind_{trail}}$	$Nu_{pole_{trail}}$
0	9710	14.8	35.4	18.5	27.3	11
779	195	10.2	25	5.7	21.4	7.3
779	795	16.1	36.6	9.9	20.5	7.8
779	1940	19.3	44.1	7.1	21.3	8.2
779	9710	29.8	67	23.2	42.1	18.3
779	29,130	39.8	107	51	64	20.3
3115	0	29.9	63.7	30.3	63.7	29.9
3115	195	25.8	56.7	25.3	56.2	24.8
3115	795	27.2	57.9	24.3	53.2	22.3
3115	1940	28.8	61.4	27.7	52.2	23.1
3115	9710	48.9	107	27.3	63.2	27.6
3115	29,130	99.2	229	66.3	117	44.8
6235	195	41	87.7	42.9	87.4	40.2
6235	795	42.9	89.4	45	85.4	37.3
6235	1940	43.6	90.3	47	82.9	35.8
6235	9710	73.3	164	51.3	88.3	40.1
6235	29,130	145	310	87.8	146	55.3

$$Nu_{notch} = 0.02 \times Re_a^{0.69} \times Re_t^{0.27} \times \left(\frac{z}{D_h}\right)^{-0.35} \quad (6)$$

The average relative error for this correlation is close to 46%, when comparing with the values of Table 6. This error is high and shows the difficulty of obtaining an accurate correlation in this region by using such this type of expression for the Nusselt number. This is particularly true when vortices are present. Nevertheless, the Nusselt number in this notch region is a function of Re_t to the power of 0.27, which is very close to the relationship found in the pole and inductive faces leading sides. Regarding the actual Reynolds number dependency (0.69), it is close to the one found by Ref. [1] (0.77).

Thus, the results from this study show that the flow and heat transfer in the notch, in the pole and inductive faces leading sides are very similar to those encountered in classical Taylor-Couette-Poiseuille flows between two concentric and smooth cylinders.

Moreover, it is interesting to compare Nusselt expressions derived from similar configurations such as a flat plate or a fixed cylinder ([13]) with those obtained for the rotor notch, as shown in Fig. 14. The correlation for a parallel air flow over a flat plate is:

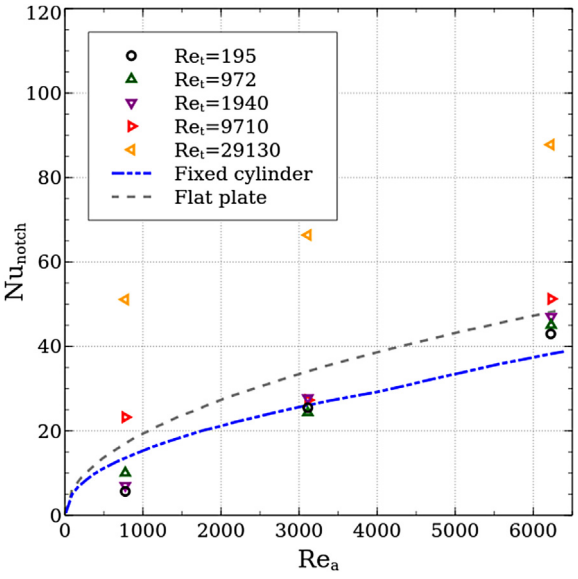

Fig. 14. Evolution of the average Nusselt number in the notch area as a function of Re_a.

$$Nu = 0.68 \times Re_a^{0.5} \times Pr^{1/3} \quad (7)$$

The correlation for a parallel air flow over a fixed cylinder is:

$$\begin{cases} Nu = 0.683 \times Re_a^{0.466} \times Pr^{1/3} & \text{for } 40 \leq Re_a \leq 4000 \\ Nu = 0.193 \times Re_a^{0.618} \times Pr^{1/3} & \text{for } 4000 \leq Re_a \leq 40000 \end{cases} \quad (8)$$

The Nusselt number values obtained in the notch region are similar to the ones observed in a flat plane or in a fixed cylinder, especially for low rotational velocities. Moreover, at a given Re_a, the value of the Nusselt number in the notch region slightly varies for $Re_t \leq 9710$ and this explains such similarity with correlation obtained on a flat plane or a fixed cylinder.

5. Conclusion and perspectives

The effect of a Taylor-Couette-Poiseuille flow in an annular channel of a slotted rotating inner cylinder was investigated in the current study. With the EDF/LAMIH-CNRS scale model of a

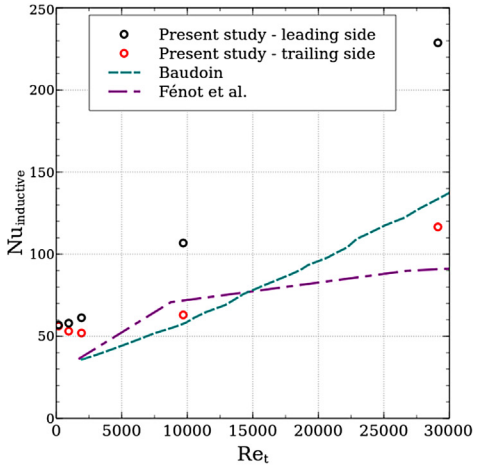

(a) $Re_a = 3115$.

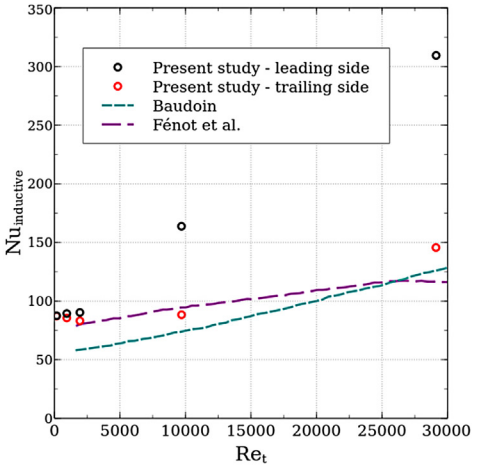

(b) $Re_a = 6235$.

Fig. 13. Evolution of the Nusselt number in the inductive faces as a function of Re_t compared to a rotating tube ([3]) and a rotating slotted cylinder ([8]).

hydrogenerator, temperatures on the rotor pole face were experimentally obtained and then compared with the numerical values calculated with Ansys-CFX and *Code_Saturne 3.0* coupled with SYRTHES 4.0, and a very good agreement was found. After this validation, a parametric analysis was performed to investigate all main flow regimes to derive expressions for the Nusselt number on the rotor pole face and sides, mainly showing that the leading edge is better cooled than the trailing edge.

These global correlations for the different rotor components can be applied to many flow regimes. However, they have to be used carefully since the accuracy of the predicted Nusselt number decreases for flow regimes where vortices are present. This limits the use of a correlation of the form: $Nu = A \times Re_a^n \times Re_t^m \times \left(\frac{z}{D_h}\right)^o$ for this type of geometry.

Moreover, the results have shown that the heat transfer in the pole and inductive faces trailing sides is quite similar to the one encountered in classical Taylor-Couette-Poiseuille flows between two concentric and smooth cylinders and that the Nusselt number dependency on Re_t is close to the theoretical value of 1/7. The same remark can be made for the dependency of the Nusselt number on Re_a in these regions, close to the literature value of 0.77.

The Nusselt number in the notch region is a function of Re_t to the power 0.27, which is very close to the relationship found in the pole and inductive faces leading sides (these regions are more affected by the tangential velocity than the trailing sides).

In the near future, an inverse method based on temperature measurements will be applied to obtain the Nusselt number distribution and to compare it with the numerical values (as already done in 1D by Ref. [15]). Furthermore, PIV measurements will be performed to further validate the CFD results.

Acknowledgment

This work was supported by EDF R&D with the help of financing from the Nord-Pas-de-Calais Regional Council and the European Regional Development Fund, as part of the MEDEE program.

References

[1] Aubert A, Poncet S, Le Gal P, Viazzo S, Le Bars M. Velocity and temperature measurements in a turbulent water-filled taylor-couette-poiseuille system. Int J Therm Sci 2015;90:238–47.
[2] Bach E, Mydlarski L, Torriano F, Charest-Fournier J-P, Sirois H, Morissette J-F, et al. Piv characterization of the air flow in a scale model of a hydrogenerator. In: ASME power conference, San Diego, USA; 2015.
[3] Baudoin B. Contribution à l'étude des conditions d'écoulement dans le circuit de refroidissement d'un moteur électrique de type ouvert [Ph.D. thesis]. Université de Poitiers; 1987.
[4] Bouafia M, Ziouchi A, Bertin Y, Saulnier JB. Étude expérimentale et numérique des transferts de chaleur en espace annulaire sans débit axial et avec cylindre intérieure tournant. Int J Therm Sci 1999;38:547–59.
[5] Carew NJ. Experimental determination of heat transfer coefficients of salient pole rotors. Therm Asp Mach 1992:1–8.
[6] Chaaban M, Leduc J, Hudon C, Nguyen DN. Thermal behaviour of large hydrogenerators. In: International symposium on Transport phenomena and dynamics of rotating machinery, 12; 1–7; ISROMAC; 2008. p. 154.
[7] Chemin S. Étude des interactions thermiques fluide-structure par un couplage de codes de calculs [Ph.D. thesis]. Université de Reims Champagne-Ardennes; 2006.
[8] Fénot M, Dorignac E, Giret A, Lalizel G. Convective heat transfer in the entry region of an annular channel with slotted rotating inner cylinder. Appl Therm Eng 2013;54:345–58.
[9] Filipan V, Budin R, Mihelic-Bogdanic A. Air flow measurement on hydro generators. Water Power Dam Constr 1993;45:44–6.
[10] Hartono E. Experimental study of air flow in a hydro power generator model [Master's thesis]. Chalmers University of Technology; 2011.
[11] Hemery G, Kunz T. Performance improvements of hydro generators due to advanced ventilation calculations. Tech. rep.. 2009.
[12] Huang CH, Lo HC. A three-dimensional inverse problem in estimating the internal heat flux of housing for high speed motors. Appl Therm Eng 2006;26:1515–29.
[13] Incropera FP, DeWitt DP. Fundamentals of heat and mass transfer. John Wiley and Sons; 2002.
[14] Jakoby R, Kim S, Wittig S. Correlations of the convection heat transfer in annular channels with rotating inner cylinder. J Eng Gas Turbines Power 1999;121:670–7.
[15] Lancial N, Beaubert F, Harmand S, Rolland G. Effects of a turbulent wall jet on heat transfer over a non-confined backward-facing step. Int J Heat Fluid Flow 2013;44:336–47.
[16] Lancial N, Torriano F, Beaubert F, Harmand S, Rolland G. Study of a Taylor-Couette-Poiseuille flow in an annular channel with a slotted rotor. In: XXIth international conference on electrical machines (ICEM), Berlin, Germany, Berlin (Germany); 2014.
[17] Lang H, Kral Ch, Haumer A, Haigis M, Schulz R. Investigation of the thermal behavior of a salient pole synchronous machine. In: Proceedings of the 17th international conference on electrical machines (ICEM), Chania (Greece); 2006.
[18] Molki M, Astill KN, Leal E. Convective heat-mass transfer in the entrance region of a concentric annulus having a rotating inner cylinder. Int J Heat Fluid Flow 1990;11:120–8.
[19] Murata K, Nonaka S, Yamamoto M, Takeda Y. Experimental study on cooling of rotor in a salient 4-pole synchronous machine. IEEE Trans Power Appar Syst 1979;98:310–7.
[20] Peres I. Contribution à l'analyse de l'écoulement et des transferts convectifs dans un espace annulaire lisse ou encoché par voie de simulations numériques [Ph.D. thesis]. Université de Poitiers; 1995.
[21] Pickering SJ, Lampard D, Shanel M. Modelling ventilation and cooling of the rotors of salient pole machines. In: IEEE-IEMDC, Cambridge, MA; 2001.
[22] Robinson W, Tse FS. Surface heat-transfer coefficients of salient poles in a blast-cooled alternator. Trans AIEE 1957;76:199–204.
[23] Shanel M, Pickering SJ, Lampard D. Conjugate heat transfer analysis of a salient pole rotor in an air cooled synchronous generator. In: Proc. IEEE-IEMDC, Madison, Wisconsin, USA, vol. 2; 2003. p. 737–41.
[24] Tachibana F, Fukui S. Convective heat transfer of the rotational and axial flow between two concentric cylinders. Bull JSME 1964;7:385–91.
[25] Torriano F, Lancial N, Lévesque M, Rolland G, Hudon C, Beaubert F, et al. Heat transfer coefficient distribution on the pole face of a hydrogenerator scale model. Appl Therm Eng 2014;70:153–62.
[26] Ujiie R, Arlitt R, Etoh H. Application of computational fluid dynamics (CFD) on ventilation-cooling optimization of electrical machines. Rev Energy Technol Gener Transm Distrib Electr Therm Energy 2006;4:17–22.
[27] Vogt B, Lahres S. Calculation of cooling and ventilation of large hydro generators with advanced 3d numerical methods. In: Proceedings of the international HYDRO conference, Innsbruck, Austria; 2013.